Journal of Hydrology 561 (2018) 833–847

Contents lists available at ScienceDirect

Journal of Hydrology

journal homepage: www.elsevier.com/locate/jhydrol

Research papers

The impact of non-isothermal soil moisture transport on evaporation fluxes in a maize cropland

Wei Shao[a,b], Miriam Coenders-Gerrits[b], Jasmeet Judge[c], Yijian Zeng[d], Ye Su[e,*]

[a] Key laboratory of Meteorological Disaster, Ministry of Education / Joint International Research Laboratory of Climate and Environment Change / Collaborative Innovation Centre on Forecast and Evaluation of Meteorological Disasters / School of Hydrology and Water Resources, Nanjing University of Information Science and Technology, Nanjing 210044, Jiangsu, China

[b] Water Resources Section, Faculty of Civil Engineering and Geosciences, Delft University of Technology, Stevinweg 1, P.O. Box 5048, 2600GA Delft, The Netherlands

[c] Center for Remote Sensing, Agricultural and Biological Engineering Department, Institute of Food and Agricultural Sciences, University of Florida, Gainesville, FL, USA

[d] Department of Water Resources, ITC Faculty of Geo-Information Science and Earth Observation, University of Twente, Hengelosestraat 99, 7514AE Enschede, The Netherlands

[e] Department of Physical Geography and Geoecology, Faculty of Science, Charles University, Albertov 6, 128 43 Prague 2, Czech Republic

ARTICLE INFO

This manuscript was handled by Corrado Corradini, Editor-in-Chief, with the assistance of Renato Morbidelli, Associate Editor

Keywords:
Evaporation partitioning
Soil-vegetation-atmosphere transfer model
Soil moisture and temperature dynamics
Non-isothermal moisture transport
Soil vapour flow

ABSTRACT

The process of evaporation interacts with the soil, which has various comprehensive mechanisms. Multiphase flow models solve air, vapour, water, and heat transport equations to simulate non-isothermal soil moisture transport of both liquid water and vapor flow, but are only applied in non-vegetated soils. For (sparsely) vegetated soils often energy balance models are used, however these lack the detailed information on non-isothermal soil moisture transport. In this study we coupled a multiphase flow model with a two-layer energy balance model to study the impact of non-isothermal soil moisture transport on evaporation fluxes (i.e., interception, transpiration, and soil evaporation) for vegetated soils. The proposed model was implemented at an experimental agricultural site in Florida, US, covering an entire maize-growing season (67 days). As the crops grew, transpiration and interception became gradually dominated, while the fraction of soil evaporation dropped from 100% to less than 20%. The mechanisms of soil evaporation vary depending on the soil moisture content. After precipitation the soil moisture content increased, exfiltration of the liquid water flow could transport sufficient water to sustain evaporation from soil, and the soil vapor transport was not significant. However, after a sufficient dry-down period, the soil moisture content significantly reduced, and the soil vapour flow significantly contributed to the upward moisture transport in topmost soil. A sensitivity analysis found that the simulations of moisture content and temperature at the soil surface varied substantially when including the advective (i.e., advection and mechanical dispersion) vapour transport in simulation, including the mechanism of advective vapour transport decreased soil evaporation rate under wet condition, while vice versa under dry condition. The results showed that the formulation of advective soil vapor transport in a soil-vegetation-atmosphere transfer continuum can affect the simulated evaporation fluxes, especially under dry condition.

1. Introduction

Evaporation in vegetated land consists of interception, transpiration, and soil evaporation, which is strongly coupled with dynamics in soil moisture and temperature (Blyth and Harding, 2011; Lawrence et al., 2007; Savenije, 2004). Both moisture and temperature at the soil surface mutually dictate the variations of albedo, emissivity, and vapour pressure, which can further influence energy budget and evaporation fluxes (Eltahir, 1998; Seneviratne et al., 2010). Direct observations of soil moisture transport and evaporation fluxes are impractical (Wei et al., 2017), therefore, numerical modelling is commonly used to study the physical processes of evaporation (Bittelli et al., 2008; Shao et al., 2017b). The model for energy and moisture transport in a soil-vegetation-atmosphere transfer continuum, being named as an SVAT model, is developed by incorporating theories from soil physics, vegetation physiology, and atmospheric science (Gran et al., 2011; Overgaard et al., 2006). Numerical simulations were indirectly validated by comparing the simulations of state variables with the measurements, e.g., weight of the soils, soil moisture and temperature (Moene and van Dam, 2014; Zeng et al., 2009a; Zeng et al., 2009b).

Most SVAT models have been focused on improving the

* Corresponding author.
E-mail address: ye.su@natur.cuni.cz (Y. Su).

https://doi.org/10.1016/j.jhydrol.2018.04.033
Received 1 December 2017; Received in revised form 8 April 2018; Accepted 10 April 2018
Available online 12 April 2018
0022-1694/

physiological representation for estimating vegetation water-use efficiency and biomass production (Best et al., 2011; Ivanov et al., 2008; Yin et al., 2014). Yet, the detailed interaction between soil moisture transport and evaporation fluxes in vegetated soils has not been explored because of the simplified description of soil physics in current SVAT models. For instance, evaporation in many SVAT models was calculated by analytical equations that specified pre-defined soil surface temperature and ground heat flux without involving an explicit calculation of the heat transport in the soil (Varado et al., 2006; Were et al., 2008; Zhou et al., 2006). The analytical evaporation equations may be suitable to areas covered by dense canopies, because the dense canopy could absorb most of solar radiation, and the ground heat flux is, therefore, less important compared with other energy fluxes. But for bare soil or sparsely vegetated soils, the evaporation fluxes can be strongly coupled with soil moisture dynamics under non-isothermal conditions, especially in arid or semi-arid environments (Wang et al., 2017). The errors in the predefined ground heat flux and soil surface temperature can significantly affect the energy budget (Kabat, 2004), and studies have indicated that the representation of soil hydrology and thermodynamics can affect the accuracy of calculated evaporation rates (Guimberteau et al., 2014; Kollet and Maxwell, 2008; Yu et al., 2016).

The model proposed by Philip and De Vries (1957), hereafter referring as the PDV model, can simulate both liquid water and vapour flow in vadose zone under non-isothermal condition, which has been widely-implemented in bare soils (Bittelli et al., 2008; Du et al., 2018; Fayer, 2000; Milly, 1984; Saito et al., 2006; Zeng et al., 2011a; Zeng et al., 2011b), as well as vegetated soils (Braud et al., 1995; Casanova and Judge, 2008; Garcia Gonzalez et al., 2012). The PDV model includes vapour diffusion, but neglects the advective vapour transport (i.e., vapour advection and dispersion caused by air flow). To compensate the underestimated vapour flow, the PDV model then adopts a theory of "liquid islands" and introduces an enhancement factor (Philip and De Vries, 1957), and the vapour enhancement factor can increase the vapour fluxes in soil about 3–6 times depending on the degree of soil saturation (Cass et al., 1984; Lu et al., 2011; Shahraeeni and Or, 2012). Many studies suggested that the vapour flow under relatively high saturation condition is not significant (Grifoll et al., 2005; Novak, 2016), especially when the enhancement factor be formulated by assuming that no liquid water flow occurred in soil (Lu et al., 2011). The soil moisture transport can be appropriately simulated by considering liquid water flow and advective vapour transport even when excluding the enhancement factor (Grifoll et al., 2005; Ho and Webb, 1998; Parlange et al., 1998).

The state-of-the-art vadose zone models simulate multiphase flow by solving the governing equations for water, air, vapour, and heat transport (Grifoll et al., 2005; Novak, 2016; Zeng et al., 2011b). The comprehensive description of above-mentioned soil hydrology and thermodynamics could facilitate the simulation of state variables (e.g., soil moisture and soil temperatures) and also the evaporation rate (Davarzani et al., 2014; Mosthaf et al., 2011; Smits et al., 2012). However, current applications of multi-phase flow models are often limited for bare soil, either for short-time period studies (a few days) under atmospheric conditions (Zeng et al., 2011a; Zeng et al., 2011b), or for soil column experiments in a well-controlled chamber environment (Davarzani et al., 2014; Mosthaf et al., 2011; Smits et al., 2012). The study that investigates the impact of advective soil vapour transport on moisture transport in vegetated soil is still lacking.

In this study, a non-isothermal multi-phase flow model was coupled with a two-layer energy balance model to investigate the detailed land-atmosphere interactions in vegetated soil. The proposed model was implemented to observations from a maize cropland in Florida, US, and the experimental period covered a complete maize-growing season. The detailed measurements of energy fluxes, soil moisture, and soil temperature were used for model calibration and validation. Detailed analyses were focused on:

1) simulating evaporation fluxes under different hydro-meteorological and vegetation conditions;
2) quantifying the interactions between non-isothermal soil moisture transport and evaporation fluxes; and
3) conducting a sensitive analysis to examine the impact of advective soil vapour transport on soil surface temperature and evaporation.

2. Field observation and experimental set-up

The study area is a maize cropland located at 29.5° N, 82.2° W in Florida, US, and the elevation is at 23 m above sea level. The cropland has a rectangular geometry with one side length of 183 m. The field experiment was conducted by the Remote Sensing Centre of PSREU (Plant Science Research and Education Unit) under the MicroWEX-2 project (Second Microwave Water and Energy Balance Experiment), aiming to investigate the land-atmosphere interactions during the maize growing season (Casanova and Judge, 2008; Judge et al., 2005). The soil in the experimental cropland was lake fine sand with a bulk density of 1.55 g/cm^3, and its percentages of sand, silt, and clay were 89.4%, 3.4%, and 7.1%, respectively (Casanova and Judge, 2008). The depth of groundwater table was 5 m below the soil surface. The soil moisture and soil temperature at five different soil depths of 4, 8, 32, 64, and 100 cm were measured by the Time-Domain Reflectometers probes and thermistors, respectively.

Maize was planted on 18 March 2004, i.e., day of year (DoY) 78. During the whole maize growing season from 19 March 2004 (DoY 79) to 3 June 2004 (DoY 155), irrigation was applied above the crops with a linear move sprinkler irrigation system. The irrigation together with rainfall were all considered as precipitation in this study, which were measured by tipping-bucket rain gauges at the east and west edge of the field. The meteorological forcing variables of wind speed, atmospheric temperature, and relative humidity were measured at the centre of the field, recording at a 15-min interval. Upwelling and downwelling shortwave and long-wave radiation fluxes were measured by a Kipp and Zonen CNR-1 four-component radiometer, and latent and sensible heat fluxes were collected with a Campbell Scientific eddy covariance system. Additionally, vegetation properties in terms of leaf area index (LAI) and canopy heights were measured weekly during the growing season (Fig. 1a), and the root density distribution was measured after finishing the whole experiment (Fig. 1b).

The net radiation had clear diurnal fluctuations (Fig. 2), reaching a local maximum value at mid-day and bottoming to a local minimum value at night. The daily trend of the local maximum values of net radiation showed a slightly increase during the spring period. The atmospheric temperature, which was intimately correlated with the net radiation, showed a similar trend. The relatively humidity and wind speed also showed clear diurnal patterns. Humidity was relatively lower during mid-day, while increased to higher values (80%–100%) at mid-night. In contrast, the wind speed was higher during the night while getting lower during the day.

3. Soil-vegetation-atmosphere transfer model

We developed a numerical model by coupling a soil multiphase flow model with a two-layer energy balance model to simulate energy and moisture transport in a SVAT continuum, and the basic model validation in a forest area under humid environment can be found in Shao et al., (2017b). This study focuses on explicit simulation of detailed interactions between non-isothermal soil moisture transport and evaporation fluxes, and furthermore we included the radative transfer model (for detail see Supplementary material). The shortwave radiation was calculated based on the Beer's law (Monteith and Unsworth, 2013), and the longwave radiation calculation was based on the widely-used equations in many land surface models (e.g., Bonan, 1994; Bonan et al., 2002; Ivanov et al., 2008). The calculated net radiation values were used as inputs for the two-layer energy balance equation.

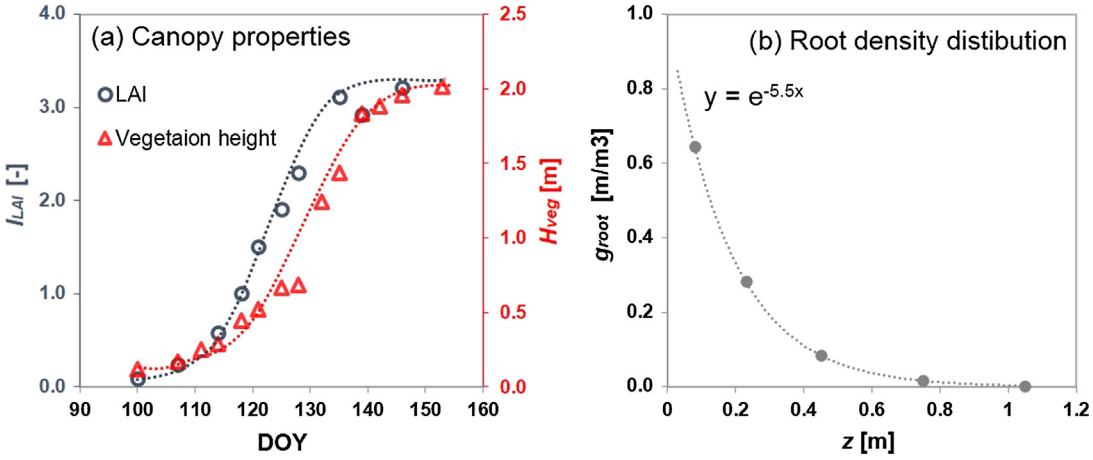

Fig. 1. a) Changes in LAI and vegetation height as a function of the maize-growing time; and b) a measured root density distribution with depth.

3.1. Two-layer energy-balance method

The net radiation of canopy layer and soil surface layer was transferred respectively to specific energy terms as (Choudhury and Monteith, 1988; Xin and Liu, 2010):

$$\mathbf{R}_{can}^{net} = \lambda E_{can} + H_{can} \quad (1)$$

$$\mathbf{R}_{sur}^{net} = \lambda E_{sur} + H_{sur} + G_H \quad (2)$$

where $\mathbf{R}^{net}$, λE, and H (W m^{-2}) are net radiation, latent heat, and sensible heat fluxes with subscripts of "can" and "sur" indicate canopy layer and soil surface layer, G_H (W m^{-2}) is the ground heat flux, E (kg m^{-2} s^{-1}) is the evaporation rate, and λ ($\approx 2.45 \times 10^6$ J kg^{-1}) is the latent heat for vaporization.

Fig. 3 shows the resistance network for calculating the energy fluxes between three interfaces – soil surface, canopy and atmosphere. The energy fluxes of sensible and latent heat are driven by gradients of atmospheric temperature and vapour pressure, respectively (Bittelli et al., 2008; Choudhury and Monteith, 1988; Xin and Liu, 2010; Zhou et al., 2006).

3.2. Canopy interception, transpiration, and root water uptake

In forested areas, interception consists of interception from the canopy and forest floor (Gerrits, 2010). The study area is maize cropland where a forest floor is not present, we therefore only included canopy interception. The interception storage can be defined as an equivalent depth of rainwater stored on leaves and branches of the vegetation canopy, and the dynamics processes can be expressed by the water balance equation (Eltahir and Bras, 1993):

$$\frac{dS_C}{dt} = (1-\tau_{rain})q_{rain} - q_{drip} - E_{int}/\rho_w \quad (3)$$

where S_C (m) is the interception storage, t (s) is the time, q_{rain} (m s^{-1}) is the rainfall intensity, E_{int} (kg m^{-2} s^{-1}) is the evaporation rate from interception, ρ_w (kg m^{-3}) is the density of water, q_{drip} (m s^{-1}) is the canopy drainage rate, $(1-\tau_{rain})q_{rain}$ is the intercepted rainwater with τ_{rain} (−) as a coefficient that denotes the fraction of rainfall directly reaching soil surface.

$$\tau_{rain} = \exp(-0.5 I_{LAI}) \quad (4)$$

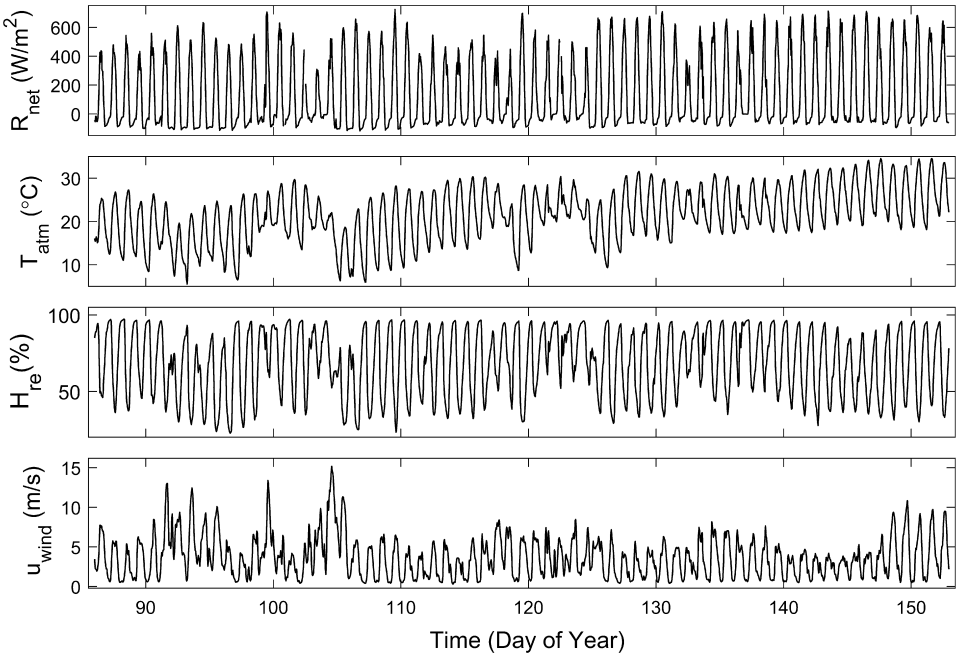

Fig. 2. Meteorological forcing data of (a) net radiation, (b) atmospheric temperature, (c) relative air humidity, and (d) wind speed during the whole study period (DoY 86–155).

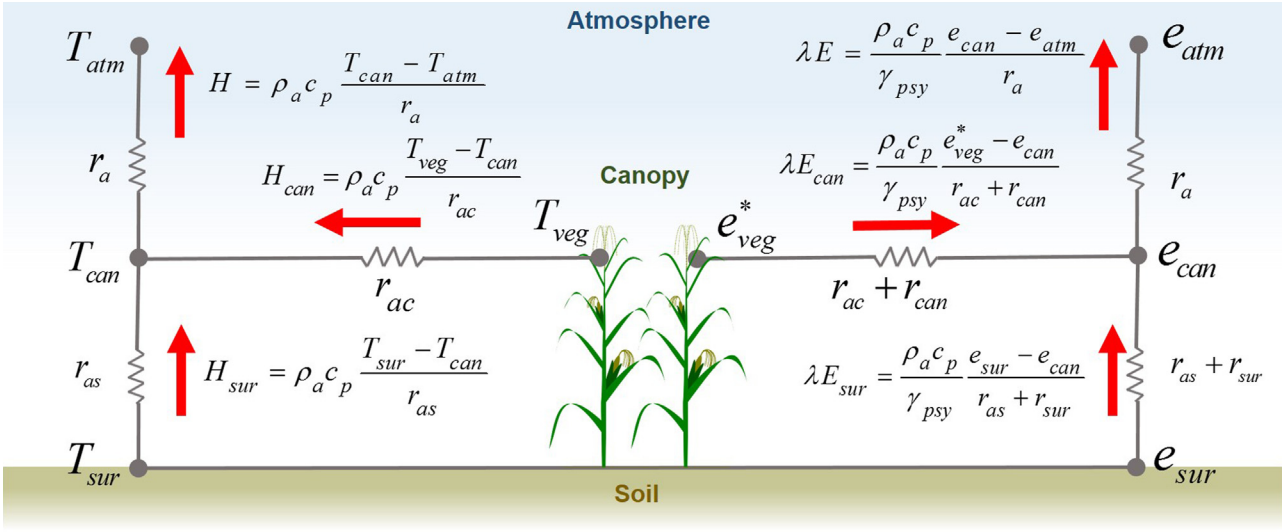

Fig. 3. Resistances network for main energy fluxes used in this study. *Notation*: T is the temperature, subscriptions of "*atm*", "*can*", "*veg*", and "*sur*" represent the atmospheric, canopy, vegetation foliage, and soil surface; ρ_a is the density of air ($=1.205\,\mathrm{kg\,m^{-3}}$); c_p ($=1013\,\mathrm{J\,kg^{-1}\,K^{-1}}$) is the specific heat capacity of moist air under a constant pressure; r_a, r_{ac} and r_{as} ($\mathrm{s\,m^{-1}}$) are aerodynamic resistances between canopy and reference height, between foliage and canopy air, and between soil surface and canopy air, respectively; γ_{psy} ($\mathrm{kPa\,°C^{-1}}$) is the psychometric constant; e^*_{veg} (Pa) is the saturation vapour pressure of air in contact with vegetation foliage, e_{can} and e_{atm} (Pa) are the vapour pressure at the vegetation canopy and the reference height, respectively, e_{sur} (Pa) is the vapour pressure at the soil surface; and r_{can} and r_{sur} ($\mathrm{s\,m^{-1}}$) are the bulk stomatal resistance and the soil surface resistance.

where I_{LAI} $(-)$ is the leaf area index (LAI).

The canopy drainage rate q_{drip} ($\mathrm{m\,s^{-1}}$) follows an exponential function:

$$q_{drip} = K_C \exp[g_C(S_C - S_{C\max})] \tag{5}$$

where g_C ($\mathrm{m^{-1}}$) is an exponential decay parameter, $S_{C\max}$ (m) is the interception capacity, and K_C ($\mathrm{m\,s^{-1}}$) is the drainage coefficient. Under heavy rainfall, canopy drainage is also affected by interception storage when assuming the interception storage shall not exceed its maximum interception capacity.

The interception evaporation E_{int} ($\mathrm{kg\,m^{-2}\,s^{-1}}$) as one component of E_{can} is related to the interception storage (van Dijk and Bruijnzeel, 2001; Varado et al., 2006):

$$E_{int} = (S_C/S_{C\max})^{2/3} E_{can} \tag{6}$$

The transpiration E_{veg} ($\mathrm{kg\,m^{-2}\,s^{-1}}$) then can be calculated with:

$$E_{veg} = E_{can} - E_{int} \tag{7}$$

E_{veg} is the actual transpiration. It drives the root water uptake that consumes soil moisture in the root zone, and the distribution of root water uptake is a function of soil moisture and root density in roots zone (Yadav et al., 2009).

Interception diminishes quantity and intensity of precipitation arriving on the soil surface, the net rainfall q_{net} ($\mathrm{m\,s^{-1}}$) that reaches the soil surface is formulated as a sum of direct throughfall $\tau_{rain} q_{rain}$ and canopy drainage q_{drip}:

$$q_{net} = \tau_{rain} q_{rain} + q_{drip} \tag{8}$$

3.3. Non-isothermal multi-phase flow in soil porous medium

The soil moisture transport in vertical direction is accompanied with processes of transporting air, liquid water, vapour, and heat in soil porous medium, which can be expressed with three mass-balance equations and one energy-balance equation respectively as (Grifoll, 2013):

$$\frac{\partial \rho_a \theta_a}{\partial t} + \frac{\partial (\rho_a q_a)}{\partial z} = Q_E \tag{9}$$

$$\frac{\partial \rho_w \theta_w}{\partial t} + \frac{\partial (\rho_w q_w)}{\partial z} = -Q_E - Q_R \tag{10}$$

$$\frac{\partial \theta_a \rho_v}{\partial t} + \frac{\partial (\rho_v q_a + \theta_a J_v)}{\partial z} = Q_E \tag{11}$$

$$\frac{\partial [\theta_w \rho_w c_w + \theta_a \rho_a c_a + (1-\phi)\rho_s c_s] T}{\partial t} + \frac{\partial [\rho_w c_w q_w + \rho_a c_a q_a + \theta_a J_v (c_v - c_{a,dry})] T}{\partial z} + \frac{\partial J_h}{\partial z} = -\lambda Q_E - c_w Q_R T \tag{12}$$

where z (m) is the vertical elevation (positive upwards); ρ ($\mathrm{kg\,m^{-3}}$) is the mass density, with subscripts of "a", "w", "v", and "s" denote air, liquid water, vapour, and solid phase, respectively; θ_w and θ_a ($\mathrm{m^3\,m^{-3}}$) are the volumetric water content (i.e., soil moisture) and the volumetric air content, ϕ ($\mathrm{m^3\,m^{-3}}$) is the porosity; Q_E ($\mathrm{kg\,m^{-3}\,s^{-1}}$) is the water phase change of vaporization and condensation, Q_R($\mathrm{kg\,m^{-3}\,s^{-1}}$) is the root uptake rate; q_w and q_a ($\mathrm{m\,s^{-1}}$) are the flow rate of liquid water and air; J_v ($\mathrm{kg\,m^{-2}\,s^{-1}}$) is the hydrodynamic dispersion of vapour flux; T (°C) is the soil temperature; c ($\mathrm{J\,kg^{-1}\,K^{-1}}$) is the specific heat capacity with different values for solids, liquid water, dry air and water vapour; and J_h ($\mathrm{W\,m^{-2}}$) is the flux rate of heat flow caused by thermal conduction and dispersion.

The specific discharge of liquid water can be calculated by the Darcy's law (Davarzani et al., 2014; Pinder and Celia, 2006)

$$q_w = -K_w \left(\frac{\partial h_w}{\partial z} + 1 \right) \tag{13}$$

where K_w ($\mathrm{m\,s^{-1}}$) is the hydraulic conductivity, and h_w (m) is the pore water pressure head. The Mualem-van Genuchten model (Van Genuchten, 1980) is used to express water retention curve and hydraulic conductivity function (given in Table 1).

In soil porous medium, the hydrodynamic vapour dispersion J_v consists of vapour diffusion and mechanical dispersion (Parlange et al., 1998):

$$J_v = -\left[\frac{D_a}{\varsigma_a} + D^M_{mG} \right] \frac{\partial \rho_v}{\partial z} \tag{14}$$

where D_a and D^M_{mG} ($\mathrm{m^2\,s^{-1}}$) are coefficients of diffusion and mechanical

Table 1
Formulation of the transport terms and coefficients.

Constitutive law	Equation	Parameter notation	Reference
Soil hydraulic function	$\Theta = \frac{\theta_w - \theta_{wr}}{\theta_{ws} - \theta_{wr}} = \begin{cases} [1 + \lvert\alpha_{VG} h_w\rvert^{n_{VG}}]^{-m_{VG}}, & h_w < 0 \\ 1, & h_w \geqslant 0 \end{cases}$ $K_w = K_{ws}\Theta^{l_{VG}}\left[1-(1-\Theta^{1/m_{VG}})^{m_{VG}}\right]^2$	θ_{wr} and θ_{ws} ($m^3\,m^{-3}$) are residual and saturation water content, Θ (−) is degree of saturation. α_{VG}, l_{VG}, m_{VG}, and n_{VG} are fitting parameters K_{ws} ($m\,s^{-1}$) is saturated water hydraulic conductivity	(Van Genuchten, 1980)
Vapour diffusion	$D_a = 2.12 \times 10^{-5}\left(\frac{T_k}{273.15}\right)^{2.0}$	T_k (K) is absolute thermal temperature	(Grifoll et al., 2005)
Vapour dispersion	$D_{mG}^M = \alpha_L \lvert v_a\rvert$	$v_a = q_a/\theta_a$ is pore velocity of air flow α_L (m) is a longitudinal dispersivity,	(Grifoll, 2013)
Thermal diffusion	$K_H = b_1 + b_2\theta_w + b_3\theta_w^{0.5}$	b_1, b_2, and b_3 are fitting parameters	(Chung and Horton, 1987)
Thermal Dispersion	$D_{mL}^H = \alpha_H \lvert v_w\rvert$	$v_w = q_w/\theta_w$ is pore velocity of water flow, α_H (m) is thermal dispersivity	(Grifoll, 2013)

Table 2
Calibrated parameters for the soil hydraulic and thermal properties.

Parameter and unit	**depth** (cm)	θ_{wr} (−)	θ_{ws} (−)	K_{ws} (m/min)	α_{VG} (m^{-1})	n_{VG} (−)
Hydraulic properties	0–50	0.003	0.34	0.012	13	1.51
	50–100	0.003	0.34	0.012	13	1.68
Thermal properties	**depth** (cm)	b_1 (−)	b_2 (−)	b_3 (−)	α_L (cm)	α_H (cm)
	0–100	0.22	−2.4	4.9	5	2

dispersion (see Table 1), and ς_a (−) is the tortuosity (Grifoll, 2013):

$$\varsigma_a = \phi^{2/3}/\theta_a \tag{15}$$

The thermal conduction and dispersion in soil porous medium is expressed as:

$$J_h = -[K_H + \theta_w\rho_w c_w D_{mL}^H]\frac{\partial T}{\partial z} \tag{16}$$

The equation expressing the thermal dispersion coefficient D_{mL}^H ($m^2\,s^{-1}$) and the thermal diffusivity K_H ($W\,m^{-1}\,K^{-1}$) are given in Table 1.

4. Model implementation and parameterization

4.1. Numerical strategies

The numerical model was codified by a Python 2.7 script. The

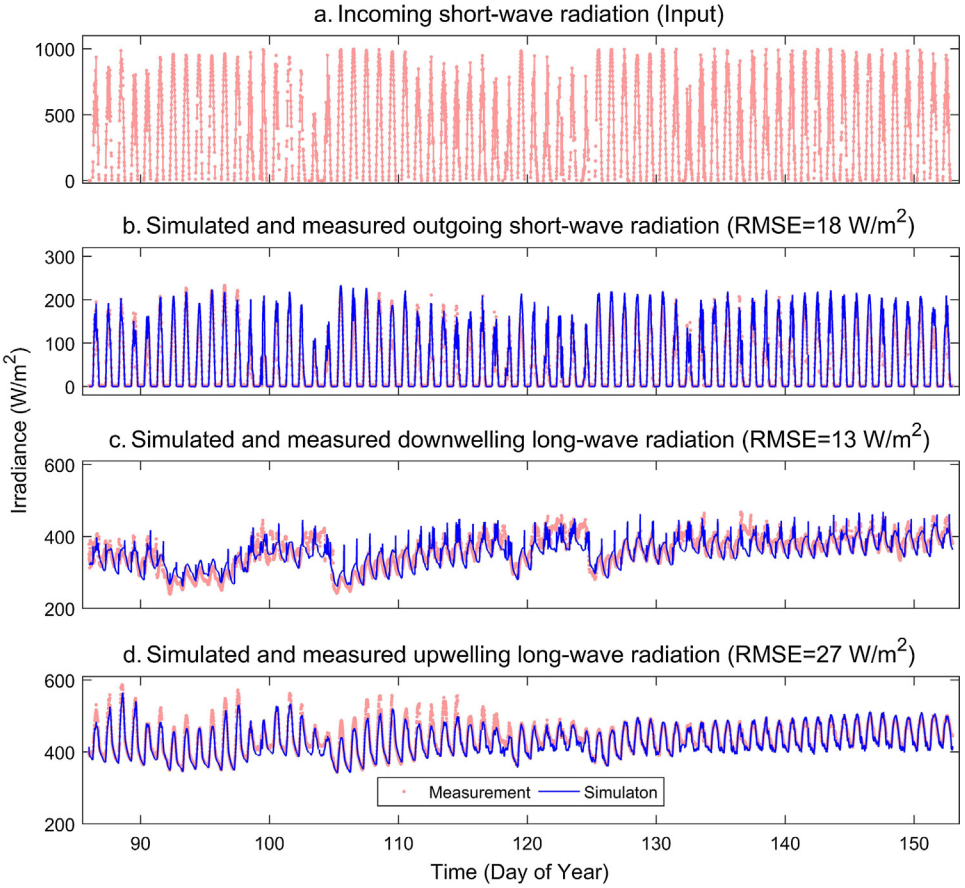

Fig. 4. a) Forcing data of incoming short-wave irradiance; (b, c, d) simulated three radiation components for the whole growing period, and their RMSEs compared with measurements are given in the brackets.

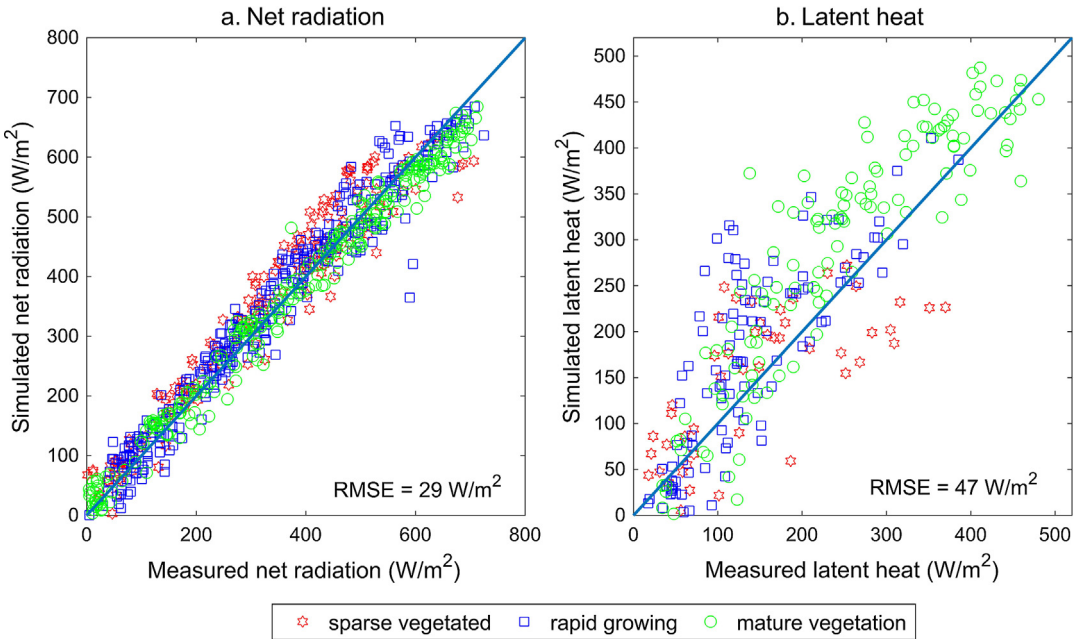

Fig. 5. Comparisons of simulated and measured net radiation and latent heat during DoY 86–DoY152. Symbols of star, square, and circle represent for the stages of sparse vegetated, rapid growing, and mature vegetation, respectively.

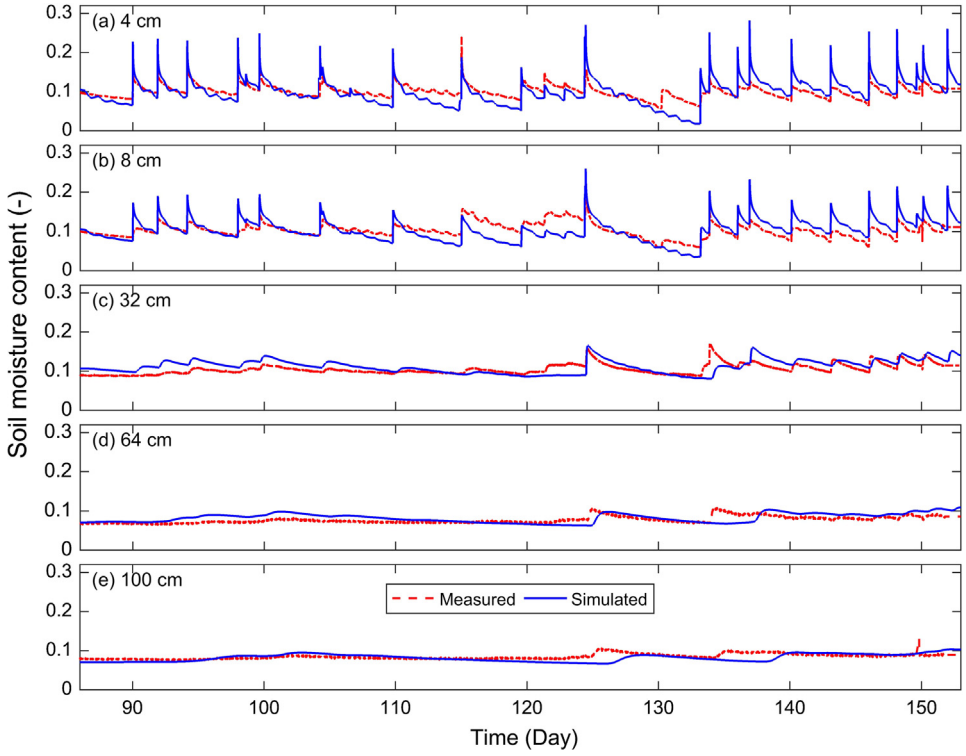

Fig. 6. Simulated and measured soil moisture content at the depth of 4, 8, 32, 64, and 100 cm below ground surface over the whole study period DoY 86–DoY152.

equations of two-layer energy balance were solved by Newton-Raphson method (Oleson et al., 2010). The soil multiphase flow model include governing equations of water, air, vapour, and heat transport. The water flow equation, combining the water balance equation and Darcy's law, is essentially the Darcy-Richards equation, which was solved by the fully-implicit finite difference approach and the Picard iteration method. The air flow equation is a first-order advection equation, which was solved by the explicit finite difference scheme. Both vapour and heat flow equations are advection-diffusion equations, which were solved by the Crank-Nicolson scheme. Those above-listed four equations composed a coupled equation system, which were solved iteratively by using Grifoll et al. (2005)'s method. The numerical errors of soil moisture and temperature were constrained by the iteration technique with tolerable errors of 0.0001 and 0.01 °C, respectively. The varying time step was in a range of 0.005–5 min to ensure sufficient computational efficiency.

The computational domain of the maize cropland was defined as the upper 1 m soil, and the discretization used a non-uniform mesh with 90

Table 3
Comparison of the RMSE and bias between the estimated soil moisture content and the measurements at the depth of 4, 8, 32, 64, and 100 cm below surface for three vegetation stages respectively.

Depth, cm	DoY 86–DoY 100 Stage 1 (sparse vegetated)		DoY 101–DoY 132 Stage 2 (rapid maize growing)		DoY 133–DoY 152 Stage 3 (mature vegetation)	
	RMSE	Bias	RMSE	Bias	RMSE	Bias
4	0.0137	−0.0022	0.0245	−0.0130	0.0262	0.0190
8	0.0155	0.0053	0.0253	−0.0154	0.0268	0.0223
32	0.0192	0.0183	0.0124	0.0018	0.0206	0.0075
64	0.0114	0.0094	0.0105	0.0035	0.0154	0.0043
100	0.0062	−0.0024	0.0107	−0.0036	0.0120	−0.0021

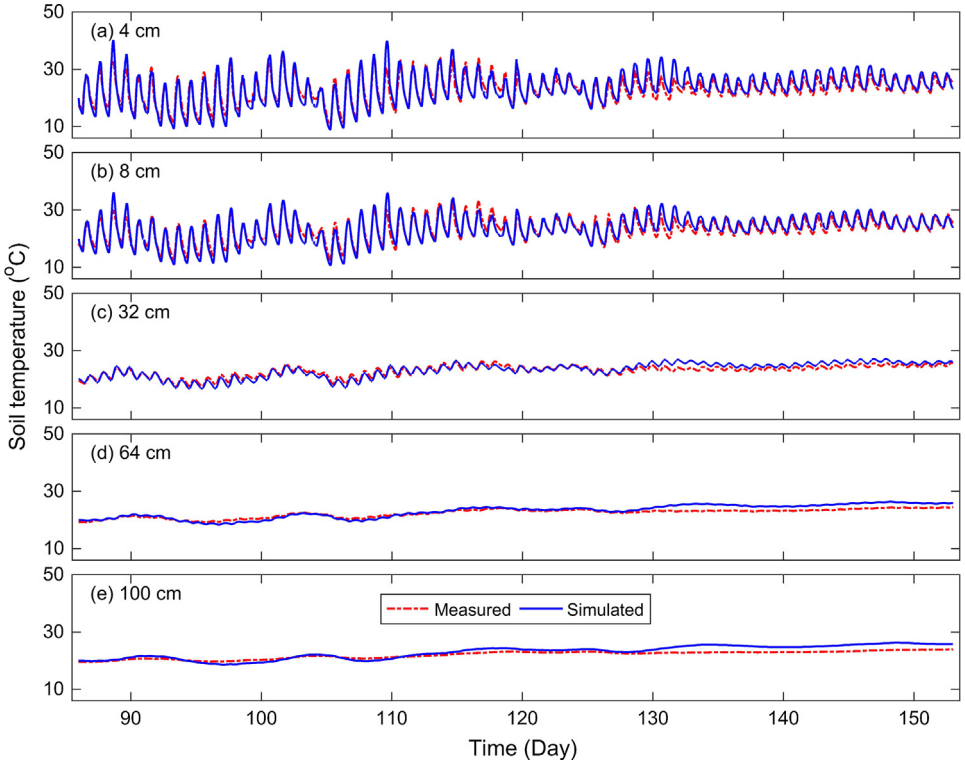

Fig. 7. Simulated and measured soil temperature at the depth of 4, 8, 32, 64, and 100 cm below the surface over the study period of DoY 86–DoY152.

Table 4
Comparison of the RMSE and bias between the estimated soil temperature (°C) and the measurements at the depth of 4, 8, 32, 64, and 100 cm below the surface for three vegetation stages, respectively.

Depth, cm	DoY 86–DoY 99 Stage 1 (sparse vegetated)		DoY 100–DoY 132 Stage 2 (rapid maize growing)		DoY 133–DoY 152 Stage 3 (mature vegetation)	
	RMSE	Bias	RMSE	Bias	RMSE	Bias
4	2.008	−0.614	2.294	0.511	1.651	1.139
8	1.741	−0.540	1.755	0.003	1.076	0.873
32	0.746	−0.455	0.958	-0.058	1.329	1.221
64	0.637	−0.156	0.757	0.264	1.833	1.473
100	0.717	−0.058	0.835	0.559	2.105	1.736

meshes and 91 nodes. The topmost soil layer (0–2 cm) was discretized with a fine mesh with 0.1 cm that facilitated the simulation of vapour transport under steep gradient of capillary pressure and temperature. The variation of soil moisture and temperature in deeper soil was not as significant as that in topmost soil layer. Therefore, the mesh size was gradually enlarged up to maximum 1 cm for the soil depth between 2 cm and 10 cm. Then, the mesh size was 1 cm for the soil depth between 10 cm and 32 cm, and 2 cm for the soil depth from 32 cm to 100 cm.

At the upper boundary of the vadose zone, the soil evaporation E_{sur} was specified for the soil vapour flow equation, and the net rainfall q_{net} was specified for the Darcy-Richards equations (Eqs. (10) and (13)). The boundary condition of soil heat flow equation (Eq. (12)) considered both thermal advection and conduction. Namely, thermal advection was driven by liquid water flow (e.g., drainage and infiltration) and air flow, and the thermal conduction at the upper boundary was set as the ground heat flux G_H.

At the lower boundary of the vadose zone, both vapour flow and air flow were specified as zero-flux. The gravitational drainage was used as a lower boundary of the Darcy-Richards equation, where the groundwater table was considered far below the computational domain. For the lower boundary of the heat flow equation, the zero-gradient condition was specified for the heat conduction term because the temperature in deeper soil (i.e., the soil depth larger than 1 m) was approximately constant during the study period.

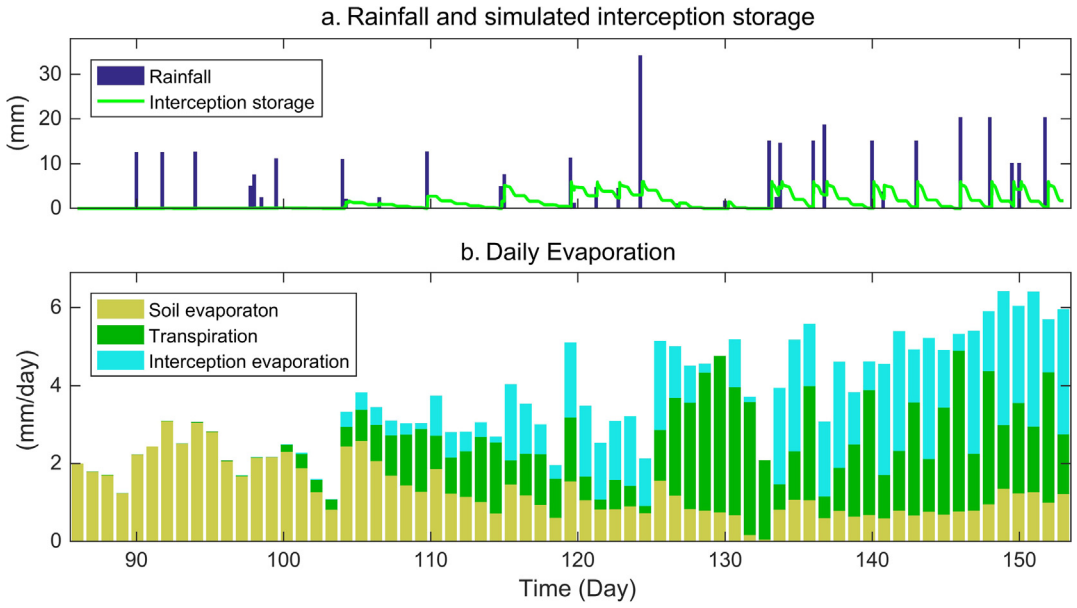

Fig. 8. (a) Input data of rainfall amount of each 6h, and simulated interception storage, and (b) daily evaporation rate, and partitioning of evaporation in soil evaporation, interception and transpiration.

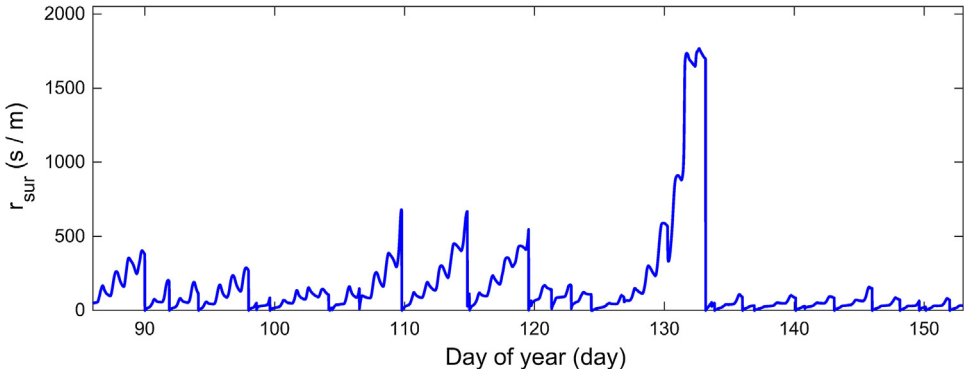

Fig. 9. Soil surface resistance over the study period DoY 86-DoY152.

4.2. Parameterization

The detailed measurements of soil properties and vegetation information in maize cropland were used to parameterize the model. The transpiration rate is related to radiation, vapour pressure deficit, leaf temperature, and soil moisture content, which quantified through the bulk stomatal resistance (Jarvis, 1976; Stewart, 1988), and the parameterization function for maize cropland was referred to Baldocchi et al. (1987). The soil evaporation rate is related to the soil moisture content at soil surface, and the soil surface resistance r_{sur} adopted an exponential function proposed by van de Griend and Owe (1994).

The soil hydraulic parameters are listed in Table 2. The saturated moisture content and saturated hydraulic conductivity were determined based on the measurement of soil samples. The parameter α_{VG} in van Genuchten model was estimated from measured air entry pressure, and n_{VG} was calibrated according to the soil moisture dynamics during the first 10 days when the soil surface was nearly barren. The measured wilting point was 0.005, and the residual water content θ_{wr} was then set to 0.003. The soil thermal parameters (Table 2) were specified as the default parameter values of sandy soil (Chung and Horton, 1987; Sakai et al., 2011). The dispersivity for vapour flow and heat flow adopt typical values suggested by Grifoll (2013).

The specified interception parameters are as follows: the maximum interception storage S_{Cmax} was set to 0–6 mm for cropland, the value is dynamic and linearly increased with LAI (Breuer et al., 2003); the canopy drainage rate K_C was set to 0.18 mm h^{-1}, and the exponential decay parameter g_C was set to 3900 m^{-1} (Ivanov et al., 2008).

4.3. Model implementation

The model was applied in the experimental cropland in Florida, US, covering an entire growing season of maize (67 days). The entire study period was split into 3 stages according to the changes in vegetation properties: a sparse vegetated period (DoY86–DoY100) when the LAI was smaller than 0.1, a rapid maize-growing season (DoY101–DoY133) when the LAI was between 0.1 and 3.0, and a mature-vegetation period (DoY133–DoY152) when the LAI gradually reached the maximum value of 3.2. For the Stage 1, the initial value of the LAI was 0.001 and the initial canopy height was set as 0.01 m to facilitate the computation. The initial condition along the soil profile was set to a uniform value: the initial temperature was set to 20 °C, and initial pressure head was set to −0.8 m.

The hourly meteorological forcing data of incoming short-wave irradiance, wind speed, atmospheric temperature, humidity, and precipitation were used as the model inputs. The model performance was evaluated by comparing the simulations with the measurements, including i) outgoing short-wave radiation, downwelling and upwelling long-wave radiation; ii) net radiation and latent heat; and iii) soil temperature and soil moisture at six depths. The root-mean-square error (RMSE) and bias were introduced as criteria:

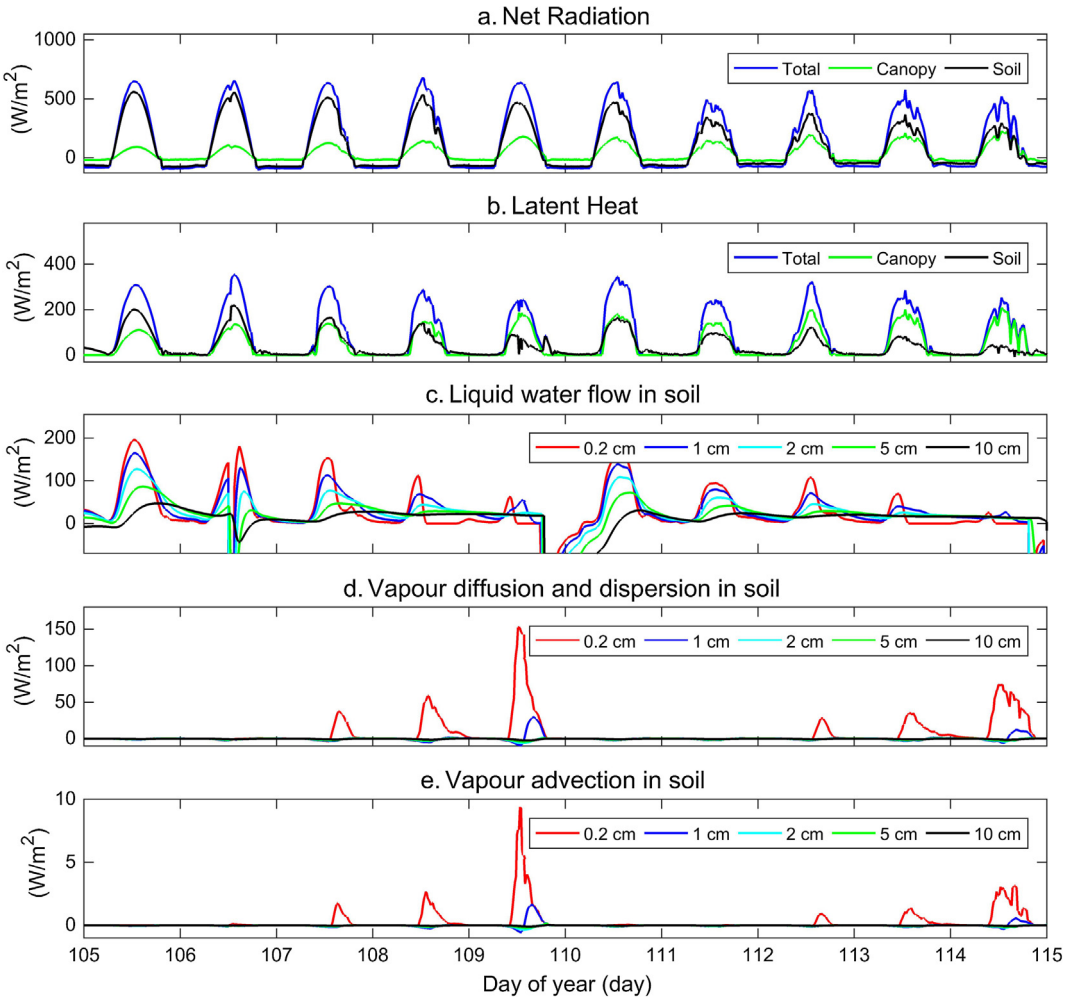

Fig. 10. Simulated energy fluxes of (a) net radiation and (b) latent heat at canopy and soil for DoY105–DoY115. The simulated (c) liquid water, (d) hydrodynamic dispersion of vapour phase (vapour diffusion and dispersion), and (e) soil vapour convection are given for the depths of 0.2, 1, 2, 5 and 10 cm below soil surface.

$$\text{Bias} = \frac{1}{N}\sum_{n=1}^{N}(\theta_{sim}-\theta_{obs}) \quad (17)$$

$$\text{RMSE} = \sqrt{\frac{1}{N}\sum_{n=1}^{N}(\theta_{sim}-\theta_{obs})^2} \quad (18)$$

5. Results and discussions

5.1. Energy fluxes

The incoming/outgoing short-wave and downwelling/upwelling long-wave irradiance are shown in Fig. 4. The incoming short-wave irradiance is a meteorological forcing variable, here only the measured values were plotted (Fig. 4a). The incoming short-wave irradiance had a clear diurnal pattern, showing the lowest value at night and the peak value during mid-day. The daily peak value of incoming short-wave irradiance has a wide range of 510–980 W m^{-2}, which were also related to the weather conditions. The daily peak values of the incoming short-wave irradiance were relatively small during rainy or cloudy weather conditions, while became much larger (e.g., 980 W m^{-2}) under clear-sky weather.

The outgoing short-wave irradiance (Fig. 4b) is related to the incoming short-wave irradiance and reflection coefficient. The reflection coefficient of vegetation foliage is approximately a constant, while the reflection coefficient of soil surface behaves as a function of moisture content at the soil surface (Casanova and Judge, 2008). A good agreement between measured and simulated out-going short-wave irradiance during the bare soil period (see Fig. 4b) provided an indirect validation of the simulated soil moisture content.

The downwelling and upwelling long-wave irradiances (Fig. 4 c, d) are functions of the temperature and emissivity of the interfaces of atmosphere, canopy foliage, and soil surface (for details see Supplementary material). The bias of incoming long-wave irradiance simulations may be caused by the uncertainties in the calculation of atmosphere emissivity and temperature (Prata, 1996; Saito et al., 2006). The upwelling long-wave irradiance depends on the land surface temperature. The under-estimation of upwelling long-wave irradiances from DoY105 to DoY120 was caused by the under-estimation of temperature of soil surface and foliage. The good agreement was achieved during Stage 3, implying the simulated foliage temperature fallen into a correct range.

The calculated hourly net radiation and latent heat fluxes were compared to the measured values (Fig. 5). It worth to notice that the latent heat fluxes during the mature vegetation period were commonly larger than the sparse vegetated period, even though the net radiation did not show such pattern. The estimated net radiation in Fig. 5a showed a consistence with the measurements (RMSE = 29 W m^{-2}), and the scatters were clearly laid on the 1: 1 line. The RMSE between measured and simulated latent heat flux was 47 W m^{-2} (Fig. 5b). The model provided reliable simulations of net radiation and latent heat under the fluctuations of meteorological condition and vegetation

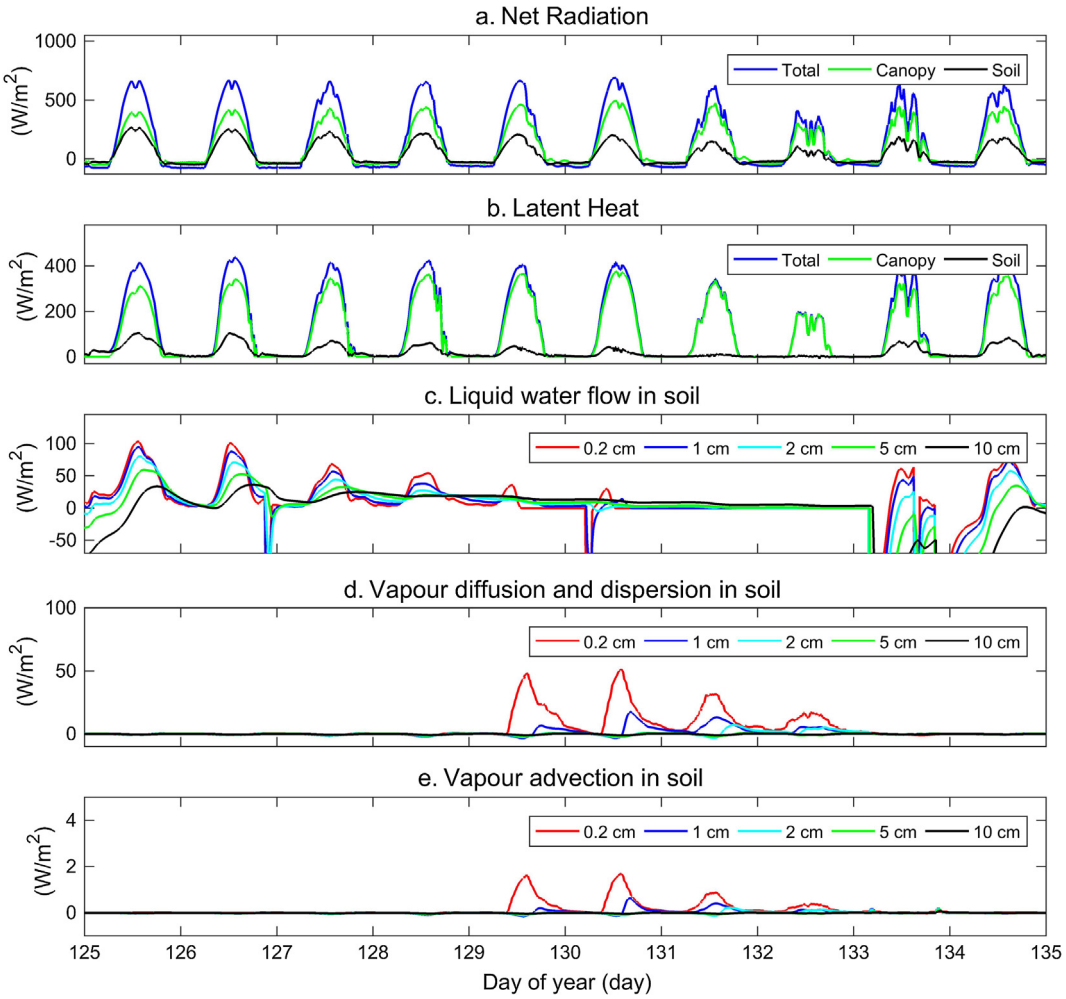

Fig. 11. Simulated energy fluxes of (a) net radiation and (b) latent heat at canopy and soil for DoY 125–DoY 135. The simulated (c) liquid water, (d) hydrodynamic dispersion of vapour phase (vapour diffusion and dispersion), and (e) soil vapour convection are given for the depths of 0.2, 1, 2, 5 and 10 cm below soil surface.

dynamics.

5.2. Soil moisture and temperature

The measured and simulated soil moisture at 5 different soil depths are shown in Fig. 6. In response to rainfall and evaporation, the magnitudes of soil moisture dynamics were much larger in upper-layer soil than in deep-layer soil. The soil moisture content at 4 cm and 8 cm depths varied in a similar range between 0.01 and 0.28. The magnitudes of soil moisture dynamics below 32 cm were much smaller with values less than 0.05. The soil moisture at 4 cm, 8 cm, and 32 cm increased sharply in response to rainfall, while decreased gradually during dry-down period due to multiple effects of evaporation, root water uptake, and drainage. During rainfall periods, the soil moisture dynamics revealed the propagation of wetting front, which was attenuated along the depth. A fraction of infiltrated rainwater was stored in the upper-layer soil (i.e., 4 cm, 8 cm) that caused the variation of soil moisture content, consequently less rainwater could reach deeper soil. During dry-down periods, soil evaporation drove exfiltration and vapour flow (detailed results will be provided in Section 5.4), and their impact was less significant at deeper depth especially below 32 cm. Similarly, the root water uptake was more significant in the upper layers soil than in deep-layer soil due to the roots distribution.

The errors statistics of simulations are provided in Table 3. The RMSEs and absolute values of bias of simulated soil moisture at all depths were less than 0.03 and 0.02, respectively, which showed the acceptable accuracy of simulation. For rainfall periods, the simulated soil moisture content well represented the hydrological response at 4 cm and 8 cm soil depth, but with significant time delays in deep-layer soil (e.g., with 5 h at 64 cm, and around 1 day at 100 cm soil depth). The under-estimation of the simulated soil moisture in deeper soil (i.e., 64 cm and 100 cm) might be a signal of the occurrence of preferential flow in sandy soil. The preferential flow can transport water with velocities much larger than that in the micropores (Shao et al., 2016; Shao et al., 2017a), and the arriving time of infiltrated water below depth of 32 cm would be much earlier than the modelling results.

The measured and simulated soil temperatures are shown in Fig. 7. The soil temperature showed a typical diurnal pattern. The amplitudes of soil temperature were decreasing along with the depth. Specifically, the amplitudes of diurnal soil temperature dynamics at 4 cm depth can be larger than 20 °C during the Stage 1. The difference in soil temperature at the depths of 64 cm and 100 cm was not significant, which was approximately equal to the average soil temperature, and the diurnal variation was less than 3 °C (Fig. 7).

The amplitudes of diurnal cycle of soil temperature were mutually affected by meteorological forcing data, LAI, and soil moisture. Compared with clear-sky periods, rainfall periods were accompanied with lower solar radiation and lower atmospheric temperature, and the infiltration then increased the soil moisture content and the heat capacity. Consequently, the amplitudes of soil temperature dynamics were lower during the rainfall period. As maize growing (i.e., LAI increasing), more solar radiation was received by canopy instead of

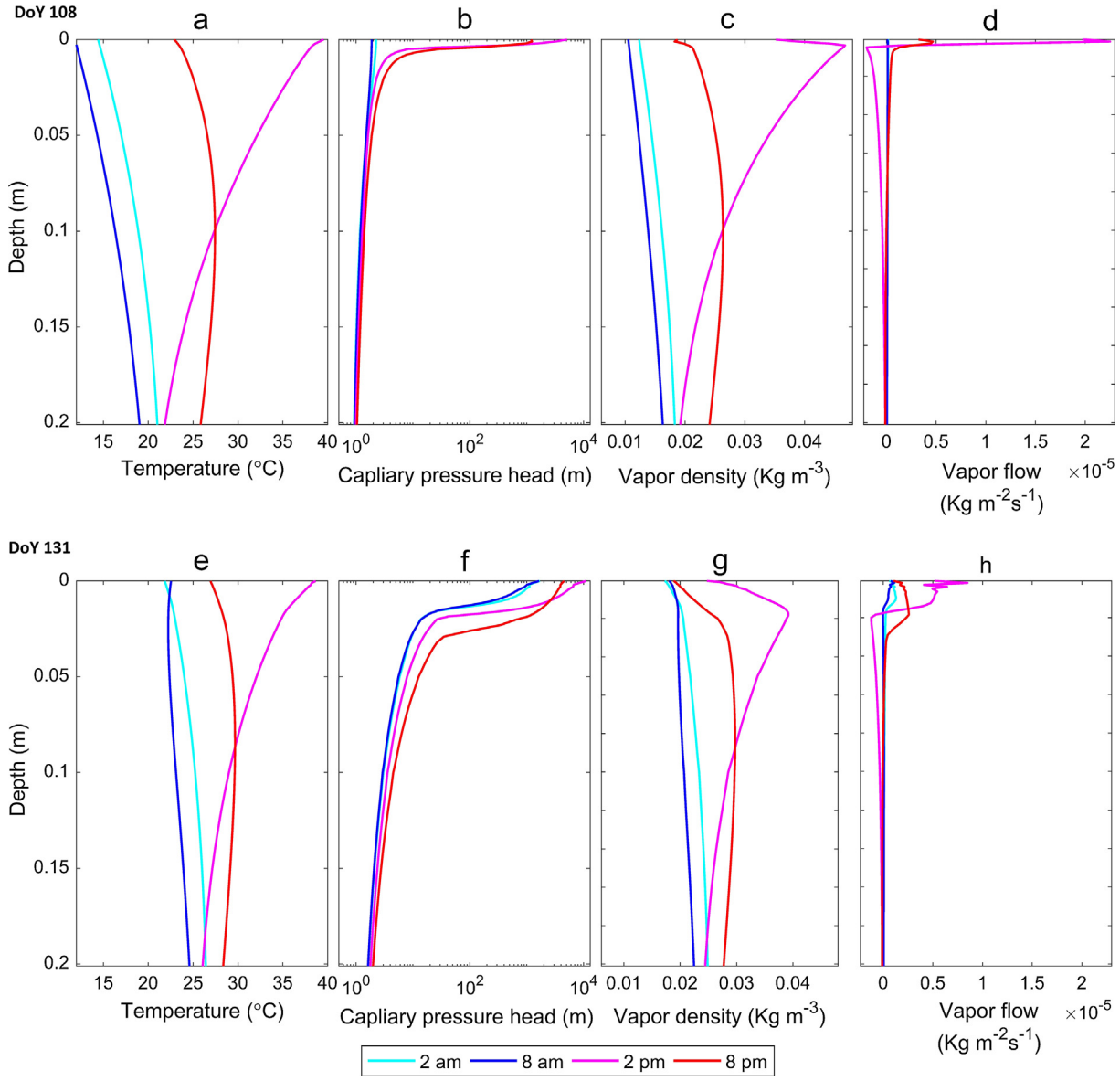

Fig. 12. Vertical profiles of soil temperature, capillary pressure head, vapour density, and vapour flow rate of the topsoil layer (0–20 cm) at 2 am, 6 am, 2 pm and 6am on two selected days: DoY108 (upper column) and DoY131 (lower column).

reaching soil surface. The amplitudes of soil temperature dynamics during the Stage 3 (when LAI > 3) were much lower compared with that during the Stage 1 and 2. For instance, the amplitudes of soil temperature dynamics at 4 cm depth were reduced from around 20 °C during the Stage 1 to less than 10 °C during the Stage 3.

The RMSE and bias of the simulated soil temperature were provided in Table 4. At 4 cm depth, the values of RMSE were around 2.0 °C, and the absolute values of the bias were around 1.0 °C. On the contrary, the RMSE and bias of the soil temperature at deeper depth (8–100 cm) were relatively smaller, namely both amplitude and daily mean values of soil temperature were well simulated. The relatively larger RMSE values of soil temperature were caused by the errors in the amplitude of diurnal variation. Such error might be related to uncertainty on the model structure, the location of the sensor (e.g., at a place with relatively low LAI comparing to the surrounding area), or the specified soil thermal properties (e.g., bulk density, thermal conductivity and heat capacity).

5.3. Evaporation partitioning

The rainfall amount of each 6 h, together with simulated interception storage S_C is shown in Fig. 8a. The S_C during the Stage 1 were negligible, while it was generally increasing along with the increasing of LAI during the Stage 2, the variation of S_C was closely related to storage capacity and rainfall (Fig. 8a). In response to rainfall, the S_C increased sharply, thereafter gradually decreased due to canopy drainage and interception evaporation. The S_C given in Fig. 8a was much higher in the Stage 3 than that was in the Stage 2, and nearly one-thirds of the rainfall intercepted during the rainfall period in the Stage 3.

The daily evaporation was expressed with equivalent depth of liquid water in mm/day in Fig. 8b, including total evaporation and its three components of interception, transpiration, and soil evaporation. Stage 1 only had soil evaporation, while during Stage 2 the impact of transpiration and interception were becoming increasingly significant. Specifically, from Stage 1 to Stage 2, the fraction of soil evaporation to total evaporation dropped from nearly 100% to less than 20% (Fig. 8). The soil evaporation component among the total evaporation was gradually replaced with transpiration and interception as LAI was continuously increasing up to 3.0. Transpiration was affected by LAI and its contribution to total evaporation was increasing during Stage 2.

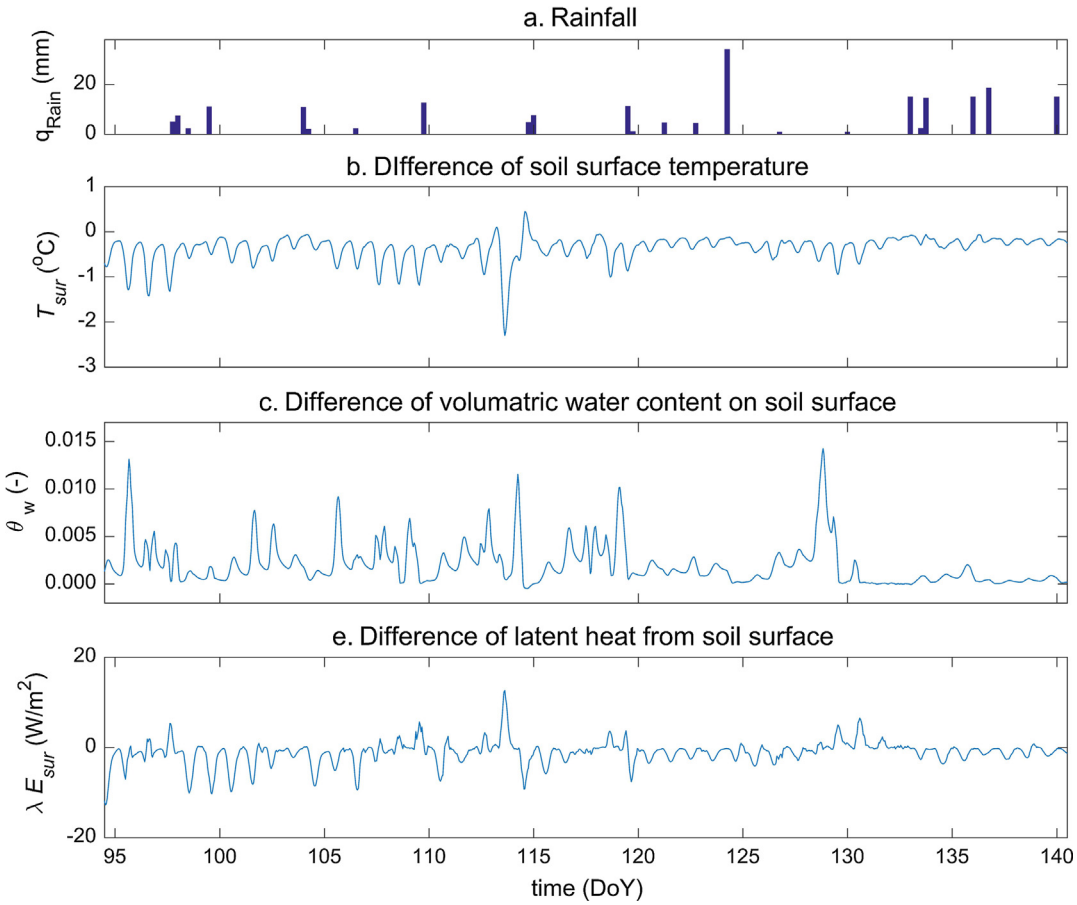

Fig. 13. (a) Input data of rainfall amount of each 6h, and (b, c, and d) simulated absolute differences (caused by including-excluding the advection and mechanical dispersion of vapour flow) of temperature, pore water pressure head, vapour density, latent heat on the soil surface, and the difference of total latent heat at the hourly step between DoY95 and DoY140.

During Stage 3, the estimated fraction of interception reached nearly 50% of the total evaporation when rainfall and irrigation occurs frequently in the study area.

The evaporation rates were correlated with the availability of energy and water. Rainfall increased the soil moisture content and provided abundant water for soil evaporation, so that the evaporation rate from wet soils was dictated by the availability of energy. During the dry-down periods, the soil moisture content in both topmost layer (i.e., 0–2 cm) and root zone layer decreased gradually. If the soil moisture was below a certain threshold, evaporation and transpiration would be hampered due to the limitation of soil moisture.

The impact of soil moisture stress on soil surface evaporation was accounted by the soil surface resistance r_{sur} as a exponential function of the soil moisture content at 1 cm depth (van de Griend and Owe, 1994). The value of r_{sur} was highly relevant to the frequency of precipitation (i.e., rainfall and irrigation). During Stage 1, the r_{sur} ranges between 10 and 600 s m^{-1} (Fig. 9). At Stage 2, both total evaporation and extraction of soil moisture increased, therefore, the topmost soil was getting dryer, which in turn led to higher value of r_{sur}. During Stage 3, the frequently applied irrigation maintained the soil moisture content at a relatively high level (Fig. 6), and thus the value of r_{sur} was also maintained in a range from 10 to 200 s m^{-1} (Fig. 9).

5.4. Interactions between energy fluxes and soil moisture transport

The simulated energy fluxes and soil moisture transport for two selected periods were shown in Figs. 10 and 11 to study the interaction between land surface and atmosphere under varying soil moisture and LAI. One period was from DoY 105 to 115, when the LAI increased from 0.2 to 1.0, and another period was from DoY 125 to DoY 135, when the LAI increased from 2.0 to 3.0. The analysis of the results of net radiation, latent heat, and soil moisture transport during these two periods can manifest the transition from a sparse vegetation period to a dense vegetation period. The results of soil moisture transport in the topsoil layer (0–10 cm) were provided, considering the soil evaporation mainly interacted with the soil moisture transport in topsoil (0–10 cm). The simulated moisture transport included liquid water flow, hydrodynamic dispersion of vapour flow (including diffusion and mechanical dispersion), and advection of vapour flow (Figs. 10 and 11). Note that the negative values of liquid water flow provided in Figs. 10c and 11c were infiltration, and the positive values were exfiltration.

Soil moisture evaporates at the surface, which drives liquid water exfiltration and an upward vapour flow in soil porous medium. The rate of soil moisture fluxes were originally expressed in unit of kg m^{-2} s^{-1}, and such rate was multiplied by the latent heat of vaporization λ ($\approx 2.45 \times 10^6$ J kg^{-1}) to express the liquid water flow and vapour flow as equivalent energy fluxes in unit of W m^{-2}. Such conversion was made based on the following considerations: (1) the Section 5.4 focused on the analysis of interaction between latent heat fluxes and soil moisture fluxes, expressing the liquid water flow with an energy flux can facilitate a direct comparison of magnitude between soil moisture transport and latent heat; and (2) both of Figs. 10 and 11 completely provided the positive value of liquid water flow to represent the exfiltration in the soil depth of 0–10 cm, and such exfiltration mainly contribute to the root water extraction or phase change in topmost soil during the intermittent period, expressing the soil moisture fluxes to energy fluxes can manifest the magnitude of soil moisture transport that potentially contributed to soil evaporation and transpiration.

The LAI affected the partitioning of solar radiation and total evaporation. During the early period of fast growing stage (DoY 105–115 in Fig. 10a), the LAI increased from 0.2 to 1.0 (see Fig. 2), and the net radiation of canopy layer increased from 10% to around 60% (Fig. 10a). The increased net radiation on canopy caused more transpiration and interception evaporation. When LAI increased to a stable value 3.2 (DoY 133–135), the canopy effectively shielded the soil surface against sunlight, so that the net radiation of canopy layer was reaching around 90%.

The liquid water flow can significantly affect both moisture transport and advective heat transfer. During the rainfall periods, the equivalent energy flux of infiltration can be several orders of magnitude larger than the exfiltration during the dry-down periods, the values exceeding the lower bound (e.g., DoY 109 in Fig. 10, DoY 133 and 134 in Fig. 11) were excluded in our analysis.

During the dry-down periods, the exfiltration delivered liquid water from deep soil to topmost soil layer for evaporation. However, the exfiltration rate decreased during the dry-down period because of the decrease in unsaturated hydraulic conductivity and soil moisture content (e.g., DoY 107–110 in Fig. 10, DoY 111–115 in Fig. 10, and DOY 125–133 in Fig. 11). In topmost soil layer (0–2 cm), if the moisture content was sufficiently low, the liquid water exfiltration in topmost soil layer (0–2 cm) was significantly decreased because the hydraulic connection in capillary flow paths was destroyed. If the liquid water flow was insufficient to transport water for soil evaporation, the soil vapour flow would start to contribute in transporting soil moisture.

The vapour flow dominate the soil moisture transport in topmost soil layer when the soil moisture content was extremely low. For instance, on DoY 109 (in Fig. 10), the vapour flow at 0.2 cm depth reached 150 $W m^{-2}$ and the water flow of exfiltration dropped to less than 100 $W m^{-2}$. Even under the dense vegetation condition (on DoY 131–132, when LAI = 2.5, see Fig. 11), the vapour flow still contributed over 60% of soil moisture transport that sustained soil evaporation. The latent heat of soil evaporation significantly decreased from 100 $W m^{-2}$ on DoY 126 to less than 30 $W m^{-2}$ on DoY 132 because the decrease of the soil moisture content (Fig. 11c), until the rainfall occurred on DoY 133 (Fig. 11b).

Generally, the results here showed two different mechanisms of soil moisture transport process. Immediately after rainfall, soil evaporation initiated at the surface and started consuming soil moisture. The upward liquid water flow (i.e. exfiltration) delivered a significant amount of water to the soil surface, contributing over 90% of soil moisture transport for sustaining evaporation, and the soil evaporation rate was primarily constrained by energy supply. When it was under the water-limited condition, the soil moisture content significantly reduced after sufficient dry-down period, during which (e.g., under soil moisture stress) the soil vapour flow dominat the upward moisture transport in topmost soils.

5.5. Diurnal variation of non-isothermal vapour flow

More detailed vertical profiles of soil temperature, capillary pressure, vapour density, and vapour flow rate on DoY 108 (when LAI = 0.2) and DoY 131 (when LAI = 2.7) were provided in Fig. 12, which illustrated the processes of soil vapour transport under both sparse and dense vegetated condition. The vapour flow under non-isothermal conditions were illustrated in Fig. 12 by showing the diurnal variation at four typical time steps (i.e., 2 am, 6 am, 2 pm and 6 pm) within those two selected days.

On DoY 108, the soil surface temperature peaked at 2 pm with a value of 40 °C and reached the lowest value of 12 °C at 6 am. The magnitude of the diurnal cycle regarding soil temperature was generally decreasing along with the soil depth (Fig. 12). The vapour transport was affected by gradients of both capillary pressure and soil temperature. The detailed simulation of vapour density profile and vapour transport revealed evaporation zone and drying front with a depth of around 1 cm. Below the drying front, the low capillary pressure head (< 10 m) along the soil profile indicated that the soil moisture was not sufficiently dry, thus the vapour flow would be dictated by soil temperature gradient. The soil vapour flow was upward during the night (e.g., 2 am– 6 am), while it was downward during the mid-day (e.g., 2 pm–6 pm). Besides, shown in the vapour flow profile of the upper panels in Fig. 12c and d, it is indicated that under wet conditions evaporation was originated from the soil surface.

On DoY 131, the amplitude of soil surface temperature was smaller than that on DoY 108 due to its larger LAI. The capillary pressure above 2 cm depth was extremely high (> 1000 m) due to low soil moisture content (which was close to residual soil moisture content). The drying front propagated downwardly to about 2 cm soil depth, above which the vapour flow was always upward driven by the capillary pressure gradient. Below the drying front, the direction of vapour flow still showed a diurnal pattern that was dictated by soil temperature variations. At night, the gradients of both soil temperature and pore water pressure head were consistently upward, which had driven upward vapour flow that transported moisture from deeper soil to the interface of drying front. During the mid-day, the vapour flow was downward that was the same direction of temperature gradient, and downward vapour flow could transport moisture to deeper soil.

5.6. Effect of incorporating the advective soil vapour transport

A sensitivity analysis was conducted to investigate the impact of different representations of soil physical processes on land-atmosphere coupling. The original results included the impact of advective soil vapour transport (i.e., mechanical dispersions and advection). In the modified modelling results, we set the air flow velocity q_a as zero to exclude the advective soil vapour transport, and only the vapour diffusion was considered.

The analysis found that there is a systematic bias from including and excluding the advective soil vapour transport for simulating latent heat flux and soil moisture/temperature (Fig. 13). The modified approach resulted in slightly lower temperature (up to 2 °C) and higher volumetric moisture content (up to 0.012) on soil surface (Fig. 13b and c). Incorporating the influence of advective soil vapour transport on soil moisture transport may lead to slightly decrease of estimated soil evaporation (around 4%) and total evaporation (around 2%).

The differences of the latent heat showed that the advective soil vapour transport can increase evaporation fluxes under dry condition. For example, the differences of latent heat fluxes on DoY 109 and DoY 129 were larger than 10 $W m^{-2}$ (6% of total latent heat), it is relacent to the soil moisture stress in a relatively short period (e.g., DoY108–109, and DoY128–132). Under extremely dry conditions, the vapour transport dominated soil moisture transport, which bring more soil moisture for sustaining soil evaporation.

In contrast, under relatively wet conditions, including the advective soil vapour transport decreased the evaporation fluxes, reflecting as about 10 $W m^{-2}$ during the Stage 1 and 5 $W m^{-2}$ during Stage 3. The results implied that an increase in soil vapour transport facilitate the upward soil moisture transport, and thus slightly increased the moisture content on soil surface. However, larger soil moisture content could result in a larger soil heat capacity, thus led to smaller amplitude of soil temperature variation during the day. A lower temperature on soil surface may lead to smaller latent heat fluxes.

6. Conclusions

The interaction between non-isothermal soil moisture transports and evaporation fluxes were quantified by the numerical modelling approach. Soil evaporation was mainly related to the soil moisture transport of topsoil layer (0–10 cm), thus was strongly affected by the dynamics of soil moisture storage in the topsoil. As the maize grows, the overall trend of total evaporation fluxes increased from 3 mm/day to

6 mm/day, while the fraction of soil evaporation decreased from nearly 100% to less than 30%. The LAI was reaching a peak value of 3.2 during Stage 3 (a maize-mature period), when the interception storage reached 6 mm. Interception played an important role in the evaporation process, especially during the rainfall period, contributing to maximum 40% of evaporation. When interception reached to zero, 70% of total evaporation was from transpiration through root water uptake from deep soil, and only 30% of total evaporation was from the soil surface.

The soil moisture transport in topmost-layer soil was either dominated by liquid water exfiltration or by vapour transport. A drying front was identified according to capillary and vapour flux profile, and it was reaching to a depth with maximum value of approximately 2 cm during the study period. Above the drying front, the hydraulic connection in capillary flow path was destroyed, which significantly diminished the liquid water flow, and the vapour flow gradually dominated the upward moisture transport. The direction of vapour flow was always upward above the drying front. Below the drying front, the direction of vapour flow showed diurnal variations that was dictated by the temperature profile, during the night the vapour flow was upward that increased the moisture content in topmost soil layer, while during the day the vapour flow was downward that was slightly exacerbating the moisture loss from the topsoil.

Finally, the impact of including advective vapour flow in the soil was quantified. The results showed that excluding the air flow effect (mechanical vapour dispersion and vapour advection) resulted in a relatively under-estimation of the soil moisture transport, which decreased the soil evaporation under wet conditions, while vice versa under dry conditions. Overall, the study showed an example of coupling the detailed soil hydrology and thermodynamic process with two-layer energy balance method, which could assist in investigating more detailed land-atmospheric interaction in vegetated area.

Acknowledgements

This research was funded by the Chinese Postdoctoral Science Foundation (No. 2017M621783), the International Postdoctoral Exchange Fellowship Program by China Postdoctoral Council (Year 2017), the Startup Foundation for Introducing Talent of NUIST (No.2017r045), the Natural Science Research Projects for Universities of Jiangsu Province (17KJB170016), the NWO Earth and Life Sciences (ALW), veni-project 863.15.022, the Netherlands.

Appendix A. Supplementary data

Supplementary data associated with this article can be found, in the online version, at http://dx.doi.org/10.1016/j.jhydrol.2018.04.033.

References

Baldocchi, D.D., Hicks, B.B., Camara, P., 1987. A canopy stomatal resistance model for gaseous deposition to vegetated surfaces. Atmos. Environ. (1967) 21 (1), 91–101. http://dx.doi.org/10.1016/0004-6981(87)90274-5.

Best, M.J., et al., 2011. The Joint UK Land Environment Simulator (JULES), model description – part 1: energy and water fluxes. Geosci. Model Dev. 4 (3), 677–699. http://dx.doi.org/10.5194/gmd-4-677-2011.

Bittelli, M., et al., 2008. Coupling of heat, water vapor, and liquid water fluxes to compute evaporation in bare soils. J. Hydrol. 362 (3–4), 191–205. http://dx.doi.org/10.1016/j.jhydrol.2008.08.014.

Blyth, E., Harding, R.J., 2011. Methods to separate observed global evapotranspiration into the interception, transpiration and soil surface evaporation components. Hydrol. Process. 25 (26), 4063–4068. http://dx.doi.org/10.1002/hyp.8409.

Bonan, G.B., 1994. A Land Surface Model (LSM Version 1.0) for Ecological, Hydrological, and Atmospheric Studies: Technical Description and User's Guide. Climate and Global Dynamics Division, NCAR.

Bonan, G.B., et al., 2002. The land surface climatology of the Community Land Model coupled to the NCAR Community Climate Model. J. Clim. 15 (22).

Braud, I., Dantas-Antonino, A.C., Vauclin, M., Thony, J.L., Ruelle, P., 1995. A simple soil-plant-atmosphere transfer model (SiSPAT) development and field verification. J. Hydrol. 166 (3–4), 213–250. http://dx.doi.org/10.1016/0022-1694(94)05085-C.

Breuer, L., Eckhardt, K., Frede, H.-G., 2003. Plant parameter values for models in temperate climates. Ecol. Modell. 169 (2), 237–293. http://dx.doi.org/10.1016/S0304-3800(03)00274-6.

Casanova, J.J., Judge, J., 2008. Estimation of energy and moisture fluxes for dynamic vegetation using coupled SVAT and crop-growth models. Water Resour. Res. 44 (7), W07415. http://dx.doi.org/10.1029/2007WR006503.

Cass, A., Campbell, G.S., Jones, T.L., 1984. Enhancement of thermal water vapor diffusion in soil. Soil Sci. Soc. Am. J. 48 (1), 25–32. http://dx.doi.org/10.2136/sssaj1984.03615995004800010005x.

Choudhury, B.J., Monteith, J.L., 1988. A four-layer model for the heat budget of homogeneous land surfaces. Q. J. R. Meteorol. Soc. 114 (480), 373–398. http://dx.doi.org/10.1002/qj.49711448006.

Chung, S.-O., Horton, R., 1987. Soil heat and water flow with a partial surface mulch. Water Resour. Res. 23 (12), 2175–2186. http://dx.doi.org/10.1029/WR023i012p02175.

Davarzani, H., Smits, K., Tolene, R.M., Illangasekare, T., 2014. Study of the effect of wind speed on evaporation from soil through integrated modeling of the atmospheric boundary layer and shallow subsurface. Water Resour. Res. 50 (1), 661–680. http://dx.doi.org/10.1002/2013wr013952.

Du, C., Yu, J., Wang, P., Zhang, Y., 2018. Analysing the mechanisms of soil water and vapour transport in the desert vadose zone of the extremely arid region of northern China. J. Hydrol. 558, 592–606. http://dx.doi.org/10.1016/j.jhydrol. 2017.09.054.

Eltahir, E., 1998. A soil moisture-rainfall feedback mechanism: 1. Theory and observations. Water Resour. Res. 34 (4), 765–776. http://dx.doi.org/10.1029/97WR03499.

Eltahir, E., Bras, R., 1993. A description of rainfall interception over large areas. J. Clim. 6 (6), 1002–1008.

Fayer, M.J., 2000. In: UNSAT-H version 3.0: Unsaturated Soil Water and Heat Flow Model. Theory, User Manual, and Examples. Pacific Northwest National Laboratory, pp. 13249.

Garcia Gonzalez, R., Verhoef, A., Luigi Vidale, P., Braud, I., 2012. Incorporation of water vapor transfer in the JULES land surface model: Implications for key soil variables and land surface fluxes. Water Resour. Res. 48 (5), W05538. http://dx.doi.org/10.1029/2011WR011811.

Gerrits, A.M.J., 2010. The role of Interception in the Hydrological Cycle. Delft University of Technology, TU Delft.

Gran, M., Carrera, J., Olivella, S., Saaltink, M.W., 2011. Modeling evaporation processes in a saline soil from saturation to oven dry conditions. Hydrol. Earth Syst. Sci. 15 (7), 2077–2089. http://dx.doi.org/10.5194/hess-15-2077-2011.

Grifoll, J., 2013. Contribution of mechanical dispersion of vapor to soil evaporation. Water Resour. Res. 49 (2), 1099–1106. http://dx.doi.org/10.1002/wrcr.20105.

Grifoll, J., Gastó, J.M., Cohen, Y., 2005. Non-isothermal soil water transport and evaporation. Adv. Water Resour. 28 (11), 1254–1266. http://dx.doi.org/10.1016/j.advwatres.2005.04.008.

Guimberteau, M., et al., 2014. Testing conceptual and physically based soil hydrology schemes against observations for the Amazon Basin. Geosci. Model Dev. 7 (3), 1115–1136. http://dx.doi.org/10.5194/gmd-7-1115-2014.

Ho, C.K., Webb, S.W., 1998. Review of porous media enhanced vapor-phase diffusion mechanisms, models, and data—does enhanced vapor-phase diffusion exist? J. Porous Media 1 (1).

Ivanov, V.Y., Bras, R.L., Vivoni, E.R., 2008. Vegetation-hydrology dynamics in complex terrain of semiarid areas: 2. Energy-water controls of vegetation spatiotemporal dynamics and topographic niches of favorability. Water Resour. Res. 44 (3), W03430. http://dx.doi.org/10.1029/2006wr005595.

Jarvis, P.G., 1976. The Interpretation of the variations in leaf water potential and stomatal conductance found in canopies in the field. Philos. Trans. R. Soc. London, Ser. B 273 (927), 593–610. http://dx.doi.org/10.1098/rstb.1976.0035.

Judge, J. et al., 2005. Field observations during the second microwave, water, and energy balance experiment (MicroWEX-2): from March 17 through June 3, 2004, tech. rep., Circular.

Kabat, P., 2004. Vegetation, Water, Humans and the Climate: A New Perspective on an Internactive System. Springer Science & Business Media.

Kollet, S.J., Maxwell, R.M., 2008. Capturing the influence of groundwater dynamics on land surface processes using an integrated, distributed watershed model. Water Resour. Res. 44 (2), W02402. http://dx.doi.org/10.1029/2007WR006004.

Lawrence, D.M., Thornton, P.E., Oleson, K.W., Bonan, G.B., 2007. The partitioning of evapotranspiration into transpiration, soil evaporation, and canopy evaporation in a gcm: impacts on land-atmosphere interaction. J. Hydrometeorol. 8 (4), 862–880. http://dx.doi.org/10.1175/JHM596.1.

Lu, S., Ren, T., Yu, Z., Horton, R., 2011. A method to estimate the water vapour enhancement factor in soil. Eur. J. Soil Sci. 62 (4), 498–504. http://dx.doi.org/10.1111/j.1365-2389.2011.01359.x.

Milly, P.C.D., 1984. A simulation analysis of thermal effects on evaporation from soil. Water Resour. Res. 20 (8), 1087–1098. http://dx.doi.org/10.1029/WR020i008p01087.

Moene, A.F., van Dam, J.C., 2014. Transport in the Atmosphere-Vegetation-Soil Continuum. Cambridge University Press.

Monteith, J., Unsworth, M., 2013. Principles of Environmental Physics: Plants, Animals, and the Atmosphere. Academic Press.

Mosthaf, K., et al., 2011. A coupling concept for two-phase compositional porous-medium and single-phase compositional free flow. Water Resour. Res. 47 (10), W10522. http://dx.doi.org/10.1029/2011wr010685.

Novak, M.D., 2016. Importance of soil heating, liquid water loss, and vapor flow enhancement for evaporation. Water Resour. Res. 52 (10), 8023–8038. http://dx.doi.org/10.1002/2016WR018874.

Oleson, K.W. et al., 2010. Technical description of version 4.0 of the Community Land Model (CLM).

Overgaard, J., Rosbjerg, D., Butts, M.B., 2006. Land-surface modelling in hydrological perspective–a review. Biogeosciences 3 (2), 229–241. http://dx.doi.org/10.5194/bg-

3-229-2006.
Parlange, M.B., Cahill, A.T., Nielsen, D.R., Hopmans, J.W., Wendroth, O., 1998. Review of heat and water movement in field soils. Soil Tillage Res. 47 (1–2), 5–10. http://dx.doi.org/10.1016/S0167-1987(98)00066-X.
Philip, J.R., De Vries, D.A., 1957. Moisture movement in porous materials under temperature gradients. Eos, Trans. Am. Geophys. Union 38 (2), 222–232. http://dx.doi.org/10.1029/TR038i002p00222.
Pinder, G.F., Celia, M.A., 2006. Subsurface Hydrology. John Wiley & Sons.
Prata, A.J., 1996. A new long-wave formula for estimating downward clear-sky radiation at the surface. Q. J. R. Meteorolog. Soc. 122 (533), 1127–1151. http://dx.doi.org/10.1002/qj.49712253306.
Saito, H., Šimůnek, J., Mohanty, B.P., 2006. Numerical analysis of coupled water, vapor, and heat transport in the vadose zone. Vadose Zone J. 5 (2), 784–800. http://dx.doi.org/10.2136/vzj2006.0007.
Sakai, M., Jones, S.B., Tuller, M., 2011. Numerical evaluation of subsurface soil water evaporation derived from sensible heat balance. Water Resour. Res. 47 (2), W02547. http://dx.doi.org/10.1029/2010wr009866.
Savenije, H.H.G., 2004. The importance of interception and why we should delete the term evapotranspiration from our vocabulary. Hydrol. Process. 18 (8), 1507–1511. http://dx.doi.org/10.1002/hyp.5563.
Seneviratne, S.I., et al., 2010. Investigating soil moisture–climate interactions in a changing climate: a review. Earth Sci. Rev. 99 (3–4), 125–161. http://dx.doi.org/10.1016/j.earscirev.2010.02.004.
Shahraeeni, E., Or, D., 2012. Pore scale mechanisms for enhanced vapor transport through partially saturated porous media. Water Resour. Res. 48 (5), W05511. http://dx.doi.org/10.1029/2011WR011036.
Shao, W., Bogaard, T., Bakker, M., Berti, M., 2016. The influence of preferential flow on pressure propagation and landslide triggering of the Rocca Pitigliana landslide. J. Hydrol. 543 (Part B), 360–372. http://dx.doi.org/10.1016/j.jhydrol.2016.10.015.
Shao, W., Ni, J., Leung, A.K., Su, Y., Ng, C.W.W., 2017a. Analysis of plant root–induced preferential flow and pore-water pressure variation by a dual-permeability model. Can. Geotech. J. 54 (11), 1537–1552. http://dx.doi.org/10.1139/cgj-2016-0629.
Shao, W., Su, Y., Langhammer, J., 2017b. Simulations of coupled non-isothermal soil moisture transport and evaporation fluxes in a forest area. J. Hydrol. Hydromechanics 65 (4), 410–425. http://dx.doi.org/10.1515/johh-2017-0038.
Smits, K.M., Ngo, V.V., Cihan, A., Sakaki, T., Illangasekare, T.H., 2012. An evaluation of models of bare soil evaporation formulated with different land surface boundary conditions and assumptions. Water Resour. Res. 48 (12), W12526. http://dx.doi.org/10.1029/2012wr012113.
Stewart, J.B., 1988. Modelling surface conductance of pine forest. Agric. For. Meteorol. 43 (1), 19–35. http://dx.doi.org/10.1016/0168-1923(88)90003-2.
van de Griend, A.A., Owe, M., 1994. Bare soil surface resistance to evaporation by vapor diffusion under semiarid conditions. Water Resour. Res. 30 (2), 181–188. http://dx.doi.org/10.1029/93wr02747.
van Dijk, A.I.J.M., Bruijnzeel, L.A., 2001. Modelling rainfall interception by vegetation of variable density using an adapted analytical model. Part 1. Model description. J. Hydrol. 247 (3–4), 230–238. http://dx.doi.org/10.1016/S0022-1694(01)00392-4.
Van Genuchten, M.T., 1980. A closed-form equation for predicting the hydraulic conductivity of unsaturated soils. Soil Sci. Soc. Am. J. 44 (5), 892–898.
Varado, N., Braud, I., Ross, P.J., 2006. Development and assessment of an efficient vadose zone module solving the 1D Richards' equation and including root extraction by plants. J. Hydrol. 323 (1–4), 258–275. http://dx.doi.org/10.1016/j.jhydrol.2005.09.015.
Wang, Z., Ankeny, M., Horton, R., 2017. The impact of water vapor diodes on soil water redistribution. J. Hydrol. 552, 600–608.
Wei, L., Dong, J., Gao, M., Chen, X., 2017. Factors controlling temporal stability of surface soil moisture: a watershed-scale modeling study. Vadose Zone J. 16 (10). http://dx.doi.org/10.2136/vzj2016.12.0132.
Were, A., Villagarcía, L., Domingo, F., Moro, M.J., Dolman, A.J., 2008. Aggregating spatial heterogeneity in a bush vegetation patch in semi-arid SE Spain: a multi-layer model versus a single-layer model. J. Hydrol. 349 (1–2), 156–167. http://dx.doi.org/10.1016/j.jhydrol.2007.10.033.
Xin, X., Liu, Q., 2010. The Two-layer Surface Energy Balance Parameterization Scheme (TSEBPS) for estimation of land surface heat fluxes. Hydrol. Earth Syst. Sci. 14 (3), 491–504. http://dx.doi.org/10.5194/hess-14-491-2010.
Yadav, B., Mathur, S., Siebel, M., 2009. Soil moisture dynamics modeling considering the root compensation mechanism for water uptake by plants. J. Hydrol. Eng. 14 (9), 913–922. http://dx.doi.org/10.1061/(ASCE)HE.1943-5584.0000066.
Yin, Z., Dekker, S.C., van den Hurk, B.J.J.M., Dijkstra, H.A., 2014. Effects of vegetation structure on biomass accumulation in a Balanced Optimality Structure Vegetation Model (BOSVM v1.0). Geosci. Model Dev. 7 (3), 821–845. http://dx.doi.org/10.5194/gmd-7-821-2014.
Yu, L., Zeng, Y., Su, Z., Cai, H., Zheng, Z., 2016. The effect of different evapotranspiration methods on portraying soil water dynamics and ET partitioning in a semi-arid environment in Northwest China. Hydrol. Earth Syst. Sci. 20 (3), 975–990. http://dx.doi.org/10.5194/hess-20-975-2016.
Zeng, Y., Su, Z., Wan, L., Wen, J., 2011a. Numerical analysis of air-water-heat flow in unsaturated soil: Is it necessary to consider airflow in land surface models? J. Geophys. Res.: Atmos. 116 (D20), D20107. http://dx.doi.org/10.1029/2011JD015835.
Zeng, Y., Su, Z., Wan, L., Wen, J., 2011b. A simulation analysis of the advective effect on evaporation using a two-phase heat and mass flow model. Water Resour. Res. 47 (10), W10529. http://dx.doi.org/10.1029/2011wr010701.
Zeng, Y., et al., 2009a. Diurnal pattern of the drying front in desert and its application for determining the effective infiltration. Hydrol. Earth Syst. Sci. 13 (6), 703–714. http://dx.doi.org/10.5194/hess-13-703-2009.
Zeng, Y., et al., 2009b. Diurnal soil water dynamics in the shallow vadose zone (field site of China University of Geosciences, China). Environ. Geol. 58 (1), 11–23. http://dx.doi.org/10.1007/s00254-008-1485-8.
Zhou, M.C., et al., 2006. Estimating potential evapotranspiration using Shuttleworth-Wallace model and NOAA-AVHRR NDVI data to feed a distributed hydrological model over the Mekong River basin. J. Hydrol. 327 (1–2), 151–173. http://dx.doi.org/10.1016/j.jhydrol.2005.11.013.